





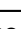


A battle against arsenic toxicity by Earth's earliest complex life forms

Received: 14 February 2025

Accepted: 5 May 2025

Published online: 19 May 2025



Anna El Khoury ^{1,2}, Andrea Somogyi ², Ernest Chi Fru ³, Farid Saleh ⁴✉, Ibtissam Chraïki ¹, Claude Fontaine¹, Jérémie Aubineau ⁵, Claire Rollion-Bard⁶, Mathias Harzhauser⁷ & Abderrazak El Albani ¹✉

The toxicity of arsenic has challenged life for billions of years, but the timing of when complex organisms first evolved strategies to cope with this threat remains elusive. Here, we study 2.1-billion-year-old (Ga) Francevillian macrofossils, some of Earth's earliest complex life forms, to establish their biogenicity and to ascertain how they managed arsenic toxicity. The studied specimens thrived in low-arsenic marine waters, yet displayed strikingly high levels of arsenic, which was actively sequestered in specialized compartments in their bodies to mitigate toxicity. Upon their death, arsenic was released and incorporated into pyrite nuclei. The patterns observed in the fossils are distinct from abiotic concretions but similar to some seen in later eumetazoans, reinforcing their biological affinity. Our findings highlight that early complex life faced significant arsenic stress, even in low-concentration marine environments, which prompted the development of essential survival mechanisms.

Arsenic (As), a toxic metalloid, exists widely in various chemical forms that influence its behavior, toxicity, environmental impact and fate^{1,2}. It occurs primarily in two inorganic forms (included herein as simplified chemical formulas): arsenite (As^{3+})—which dominates in low-oxygen environments, and arsenate (As^{5+})—common in oxygen-rich conditions³. Additionally, As can exist in organic forms, including methylated and sulfur-containing (thiolated) compounds, in living organisms and the environment⁴.

For billions of years, a narrow range of microorganisms have cycled As^{3+} for energy and growth⁵. For example, ancient microbial mats, exemplified by 2.7 Ga-old stromatolites from Western Australia⁶, have revealed how some early microbial communities thrived on As metabolism^{7,8}. Arsenic has also been associated with the Ediacaran Amana Tazgart microbialites (Anti Atlas, Morocco) that inhabited an extreme terrestrial As-rich volcanic lake^{9,10}, with modern analogs for this ecosystem being the Laguna del Diamante Lake (Argentina)^{11,12}, Mono lakes^{7,13} (USA), and the As-rich shallow submarine hydrothermal

ecosystems in the Hellenic Volcanic Arc (Greece). In these ecosystems, bacterial survival depends on strong As detoxifying mechanisms and the ability to discriminate As^{5+} from phosphate to survive^{14,15}. Current evidence suggests that some of Earth's first photosynthetic microbes may have survived entirely by oxidizing As anaerobically^{8–10}.

Regardless, As is toxic to all of life, including those that metabolize As for energy and growth gains, with eukaryotes being especially vulnerable¹. Consequently, like prokaryotes, eukaryotes have, through time, evolved some mechanisms to detoxify As intrusions into their bodies¹³. This includes the extrusion of As from the cell using As-resistant genes¹⁶, the production of low-molecular-weight chelators to prevent As from binding to physiologically important proteins, the genetic expression of highly selective cell membrane transporters to discriminate against the uptake of As^{5+} into cells and the sequestration of As in intracellular compartments to avoid damage^{17,18}. Thus, in all modern settings, life is equipped with one or a multitude of As detoxifying mechanisms to prevent As toxicity^{1,4,16,19}. This phenomenon

¹Université de Poitiers, IC2MP, UMR 7285, CNRS, 86073 Poitiers, France. ²NANOSCOPIUM beamline, Synchrotron SOLEIL, 91190 Saint-Aubin, France. ³Cardiff University, School of Earth and Ocean Sciences, CF10 3AT Cardiff, UK. ⁴University of Lausanne, Institute of Earth Sciences, Géopolis, CH-1015 Lausanne, Switzerland. ⁵Géosciences Environnement Toulouse (GET), UMR 5563 CNRS, UR 234 IRD, UM 97 UT, CNES, Observatoire Midi-Pyrénées, 31400 Toulouse, France. ⁶Université Paris-Saclay, Laboratoire des Sciences du Climat et de l'Environnement (LSCE), CNRS, CEA, UVSQ, 91191 Gif-sur-Yvette, France. ⁷Natural History Museum Vienna, Geological-Palaeontological Department, Burgring 7, 1010 Vienna, Austria. ✉e-mail: farid.nassim.saleh@gmail.com; abder.albani@univ-poitiers.fr

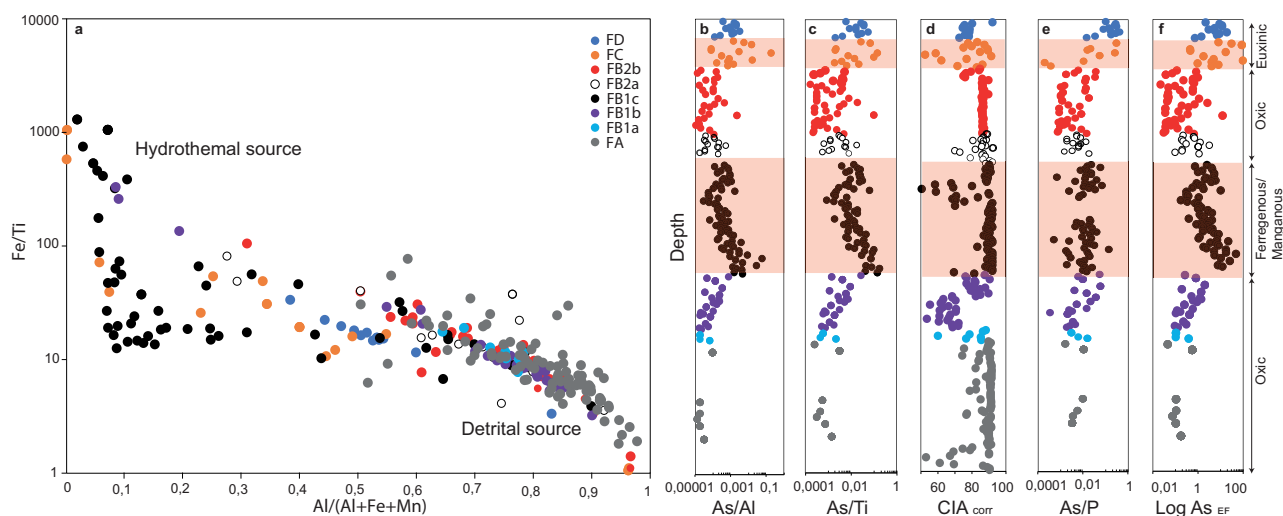


Fig. 1 | Elemental distribution and concentration in the Francevillian sediments. **a** Bulk Fe/Ti versus Al/(Al + Fe + Mn) hydrothermal proxy^{38,98} cross plot for the different units in the Francevillian stratigraphic sections. **b, c** As/Al and As/Ti ratios **d**, Chemical Index of Alteration (CIA) values illustrating the degree of

chemical weathering across different units. **e** As/P ratios across the section. **f** As enrichment factor (EF) dynamics. The FB2b unit hosts the studied eukaryotic macrofossils. The shaded orange intervals point to arsenic enrichments. Source data are provided as a Source Data file (Table S1).

suggests that circumventing As toxicity was likely pertinent and central to the evolution and survival of life in all environments throughout Earth's history.

Geochemical evidence demonstrates that active As³⁺ and As⁵⁺ detoxification in prokaryotes first emerged during Archean time, just before the Great Oxidation Event (GOE)^{20,21}, when the first permanent appearance of oxygen in the atmosphere²² coincided with the global rise of As⁵⁺ in seawater²³. However, exactly when and how complex eukaryotes developed As detoxification strategies, like storing As inside their bodies, especially in response to evolving environmental As concentrations, redox and chemistry, remain poorly understood. Efficient detoxification through As efflux pumps expels arsenic, leaving minimal traces in cells²⁴. In contrast, organisms relying on internal sequestration bioaccumulate As, leading to elevated concentrations in organisms^{17,18}. Here, we test the hypothesis that the As content of fossils, compared to enrichment in co-eval non-biological structures, coupled with a detailed understanding of environmental As cycling dynamics, speciation and redox, can reveal how ancient organisms managed As in life. Using a combination of high-resolution advanced microanalytical techniques, we constrain As enrichment patterns in the pyritized Paleoproterozoic Francevillian biota and compare these patterns with those observed in pyritized Phanerozoic eumetazoans and pyritized abiotic concretions formed under similar environmental conditions. We then identify As-enrichment patterns unique to the 2.1 Ga-old Francevillian biota²⁵, allowing to explore how these ancient complex communities of organisms managed As stress.

While debates about their biogenic origins persist^{26,27}, detailed studies of the morphology, environmental growth conditions, and geochemistry of the Francevillian biota^{28–33}, have accumulated substantial evidence on their biological affinity, placing them among the earliest complex eukaryotes, and a prokaryote affinity was disregarded^{30–32,34}. Our findings provide insights into how one of Earth's earliest eukaryotic assemblages may have adapted to toxic environmental As levels. These Francevillian organisms lived in phosphate-rich oxygenated marine waters³⁵, and relied on storing As within their bodies to circumvent toxicity. Interestingly, their limited distribution and relatively short existence of perhaps a few hundred thousand years imply that this detoxification strategy may have evolved independently in complex eukaryotes at least twice.

Results and discussion

Bulk rock As content and seawater trends

Detailed stratigraphic reconstruction of the Francevillian sub-basin and geological setting information can be found in previous publications^{28,32,36,37}, Supplementary Materials, and Fig. S1. Bulk rock As geochemistry shows distinct enrichment patterns varying across the sequence, which appears to be influenced by seawater redox depositional conditions, fluctuating hydrothermal activity, and chemical weathering of continental rocks (Fig. 1). The bulk rock As trend across the section, combined with the Fe/Ti versus Al/(Al + Fe + Mn) hydrothermal proxy^{35,38,39}, point to strong hydrothermal enrichment in the FB1c unit underlying the macrofossil yielding FB2b unit and the overlying FC Formation (Fig. 1a, f). In contrast, hydrothermal activity is not identified as a strong component of the FB2b unit—sediment and As supply being predominated instead by continental weathering³⁰ supported by chemical index of alteration (CIA) values > 80 (Figs. 1a–d, f; Supplementary Materials; Table S1). Low As/Al and As/Ti ratios point to an increase of detrital input at this time (Fig. 1b, c). While bulk As/P ratios are relatively stable across the section (Fig. 1e), As is enriched in the FB1b unit and FC Formation that are impacted by hydrothermal input³⁷ in comparison with the upper continental crust (UCC) (Fig. 1f). These enrichment calculations of As could slightly be overestimated due to a shuttle effect, but would affect all of the stratigraphic section^{40,41}. Across the sequence, a dramatic decline in As/Al and As/Ti ratios distinguishes the fossil-rich FB2b unit, while the high ratios in the FB1c unit and the overlying FC Formation, indicate a stronger authigenic source for dissolved As, coupled to submarine hydrothermalism. For example, previous evidence shows that the hydrothermal activity associated with the FB1c unit was the source of Fe and Mn in the Paleoproterozoic Francevillian Ocean³⁵, which subsequently led to the Fe–Mn-rich carbonate formation. The re-emergence of As enrichment in the FC Formation, probably related to subaerial volcanism, demonstrated by the absence of Mn and Fe deposition, coincides with bottom-water anoxia⁴² and the disappearance of the Francevillian biota (Fig. 1a).

The absence of hydrothermal contribution to the fossil-yielding FB2b unit aligns with previous findings indicating that oxidative weathering of Paleoproterozoic As-bearing minerals may have been the main source for As, introducing it from the continents to the oceans^{23,43} during the GOE. Considering that the CIA index is a climate-weathering indicator, it provides support for the proposition that

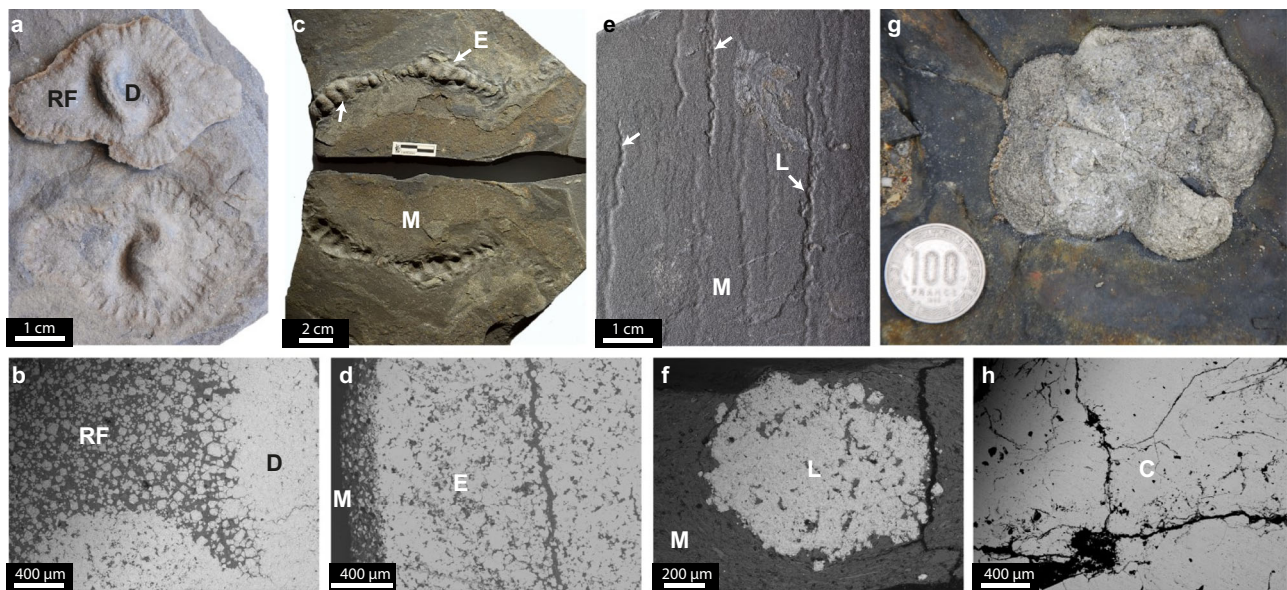


Fig. 2 | Pyritized specimens of Gabon. **a** Lobate fossil with imprint showing dispersed pyrite grains at the radial fabrics (RF) and coagulated pyrite towards the dome (D) (**b**). **c** Elongate fossil (E) in a matrix (M) with imprint surrounded by bacterial mat³¹ showing mainly coagulated pyrite crystals (**d**). **e** Tubular fossil (T) having an ovoid diameter filled with coagulated pyrite in a matrix (M) (**f**). **g** Pyritized

abiotic concretion (C) found in the same location and containing massive pyrite (**h**). The diameter of the coin in (**g**) is 3.6 cm. Scanning electron microscope is used in back-scattered electron mode in **b**, **d**, **f** and **h**. It shows pyrite grains filling the specimens in a vertical transect.

climate-driven weathering dynamics have impacted marine arsenic content throughout Earth's history^{30,43}. In well-oxygenated environments, As^{5+} is the dominant species, typically accounting for 90–100% of total dissolved As, due to rapid oxidation and higher stability than As^{3+} , particularly at circumneutral to alkaline pH^{44,45}. Moreover, reconstruction of the oxidation state of As in marine shales showed a dominance of As-S and As^{5+} species, with As^{3+} being below the detection limit²³. This further sheds light on a rapid rise in seawater As^{5+} content coinciding with the GOE and the emergence of As^{5+} detoxification genes²². Thus, in the oxidizing conditions associated with the FB2b lithologies containing the complex macrofossils³⁶ examined in this study, As^{5+} was most likely the predominant arsenic species in seawater.

Trace element content in pyritized macrofossils

Macrofossils from the Francevillien sub-basin can be broadly separated into two types: non-pyritized specimens that tend to occur abundantly on shale surfaces and pyritized specimens separated into lobate, elongated and stringed forms (Fig. 2). The lobate structures, comprised of an ovoidal inner and an outer section are composed of a succession of smaller lobes delimited by deep radial striae (Figs. 2a, 2b). The elongated specimens consist of sinuous cylinders of several centimeters in diameter (Fig. 2c, d), while the pyritized tubular or string-shaped structures are sinuous, millimetric, and ovoid in diameter (Fig. 2e, f). Abiotic pyritized concretions frequently coexist with these macrofossils (Fig. 2g, h). Further details differentiating the macrofossils from the abiotic concretions are reported elsewhere^{28–32,34}. The high Ni concentrations (1740 ppm, 1457 ppm and 730 ppm, respectively, for the tubular, lobate, and concretions), obtained by laser-ablation (LA)-ICPMS, along with the low Co/Ni ratios (Fig. 3a, b; Table S2), indicate that an organic matter-rich depositional environment under reducing conditions^{46,47} supported sedimentary pyrite formation^{48,49}. This interpretation is corroborated by the Ag/Au and Bi/Au ratios >1 in all samples, in addition to high As/Au ratios >200 and low As/Ni and Zn/Ni ratios <10 (Fig. 3a). This confirms the diagenetic origin of these pyrites^{49,50}. However, the diagenetic timing of pyrite formation in macrofossils and abiotic concretions differs. The taphonomic process of macrofossil preservation involved rapid, early

authigenic pyritization, which prevented the loss of anatomical details and replicated their morphology during decay in early diagenesis²⁹. In contrast, pyrite in abiotic concretions exhibits signs of recrystallization and is thought to have precipitated later, at least partially, during late diagenesis^{29,30,51}.

This interpretation is further supported by trace element data, which show that As, Ni, Pb, Cu, Co, and Mn are the most enriched elements in the lobate and tubular macrofossils as well as in concretions, followed by Sb, Zn, Se, and Mo, despite elements like As being relatively lacking in the bulk rock FB2b unit in comparison to other units of the formation. Silver, Bi, Cd, and Au are the least enriched elements in all specimens (Fig. 3b, Table S2). However, the elemental content in the lobate and tubular fossil specimens is generally higher than that observed in the abiotic concretions (Fig. 3b). The enrichment of trace elements in pyrite within the macrofossils, compared to the abiotic concretions, correlates with the abundance of light sulfur isotopes in the former²⁹. This further supports an early diagenetic source of pyrite in the macrofossils. In other words, pyrite grains in the fossils were formed by the activity of sulfate-reducing microorganisms during early diagenesis, while pyrite in concretions formed later during late diagenetic processes^{29,30}.

Arsenic enrichment in pyrite

Our geochemical analysis confirms previous observations suggesting macrofossil preservation in the FB2b unit took place under sulfate-reducing early diagenetic conditions²⁹. Compared with the pyritized abiotic concretions, a unique As distribution pattern is observed in the individual pyrite crystals (30 μm in length) associated with the macrofossils. In these fossils, As uniquely forms the core of the pyrite crystals (Fig. 4a–d, 5a–d; Fig. S2). This is interpreted to imply that As was central to initiating the pyritization process, via catalyzing pyrite precipitation in the biological specimens, as observed in modern pyrite precipitation experiments where metals are shown to expedite the process of pyrite precipitation⁵². The concentration of As generally decreases with increasing distance from the core of the pyrite grains in the macrofossilized specimens (Figs. 4e–g, 5e–g; Figs. S3–S5), indicating that As was not always available for pyrite growth, and had a

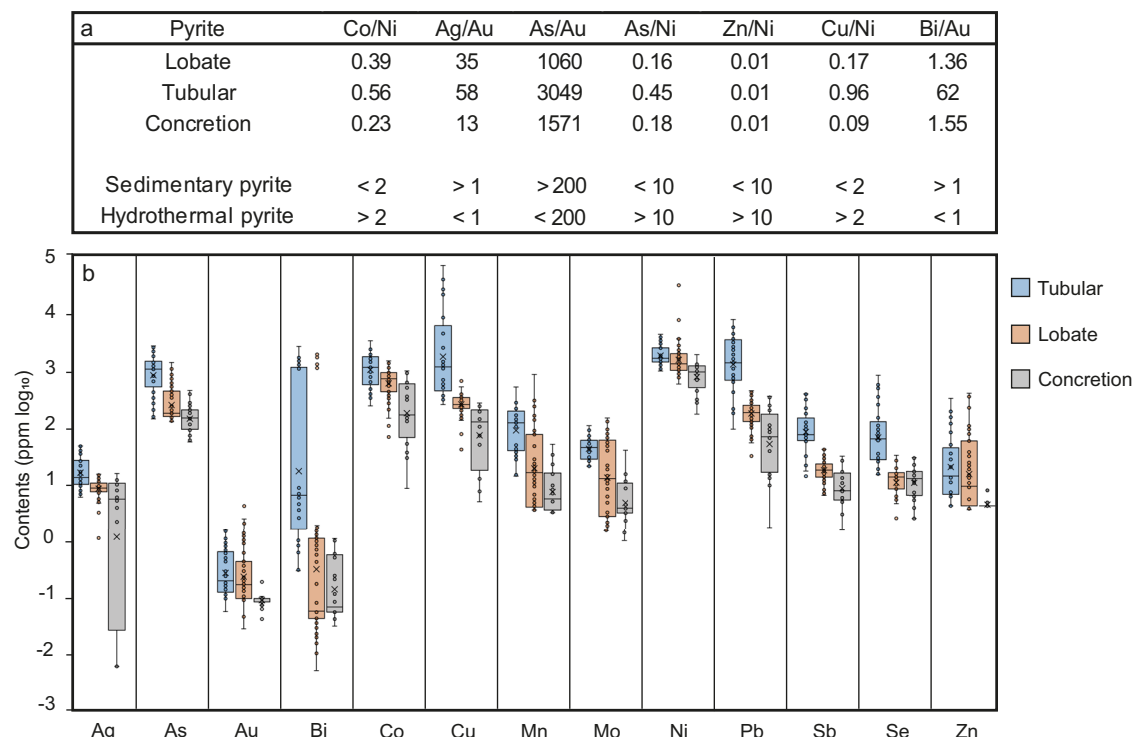


Fig. 3 | Elemental distribution and concentration in Francevillian fossils. a The characteristic ratios of trace element content (ppm) in sedimentary and hydrothermal pyrite⁴⁹ confirm the sedimentary formation of pyrite in all of the Gabonese specimens. **b** Comparative boxplot of LA-ICPMS analysis of trace element concentrations in pyrite from the tubular fossils, lobate fossils, and the abiotic concretions, showing trace element enrichment in fossils compared to the late

diagenetic pyrite concretions. The median is represented by a line inside the box, which itself represents the interquartile range (IQR) (Q1, 25th percentile and Q3, 75th percentile). Whiskers extend to the minimum and maximum values within 1.5 IQR. Points are the outliers. Source data are provided as a Source Data file (Table S2).

limited concentration within the decay microenvironment. Arsenic content in these pyrites correlates with the concentration of Ni and Cu (Figs. 4g–i, 5g–i). On the contrary, pyrite in the abiotic concretions is massive (Fig. 4j, k) and As is either absent or displays a diffuse or hotspot behavior within the pyrite, with no apparent zonation or nucleus-like structure (Fig. 4l). In these concretions, Ni and Cu are diffusely distributed within the pyrite grains but absent at the edges (Fig. 4m, n), following the same pattern of distribution and showing no correlation with As. The matrix between the pyrite grains does not contain As (Fig. 4o). Moreover, the tube and lobate fossils are significantly more enriched in As, obtained by (LA)-ICPMS, than the abiotic concretions (ANOVA F -statistic = 36.58, p -value = 1.45×10^{-12}).

A comparison of our observations with the As distribution in pyritized Phanerozoic eumetazoan fossils demonstrates that As is indeed present in most of these fossils (a detailed and referenced description is provided in the Supplementary material; Figs. S6–S8), with some exhibiting enrichment patterns akin to those recorded in the Francevillian specimens and principally associated with pyrite nuclei and sometimes linked to Fe alone [when sulfur has been leached from pyrite; e.g., *Coeloma rupeliense*, (Decapoda, Bilzen formation, Belgium, Rupelian⁵³; Fig. S6) and *Penaeoidea indet.*, (Decapoda, La Voulte sur Rhône, France, Callovian⁵⁴; Fig. S7)]. However, this is not a uniform pattern observed in all Phanerozoic eumetazoans. Some eumetazoans do show As enrichment but not in association with pyrite nuclei (e.g., *Ecrinaster roemeri*, *Echinodermata*, Hunsrück, Germany, 400 Ma; Fig. S8), meaning that As enrichment in some eumetazoans is likely the result of complex fluid circulation over geological time rather than early diagenesis.

More important than this comparison with Phanerozoic eumetazoans is that As incorporation in the macrofossils differs significantly from As patterns and distribution in abiotic concretions despite both

Francevillian macrofossils and abiotic concretions coming from the same sedimentary unit. If As incorporation in fossils was solely due to abiotic processes over geological time, a similar As distribution pattern would be expected in both the macrofossils and abiotic concretions, which formed in the same sedimentary layer and experienced similar burial processes^{55,56}. Moreover, the pattern of As enrichment would be different if its incorporation was solely linked to processes such as metamorphism, hydrothermalism, or late diagenesis. In such scenarios, the opposite pattern to what is observed here would be expected with the enrichment of As at the borders of pyrite crystals⁵⁷, where fluids circulate, and a decreasing concentration toward the center of the crystals^{55,58,59} (Fig. 6a–d). Instead, the incorporation of As into pyrites in the Francevillian macrofossils must have occurred at the same time as pyrite nucleation during early diagenesis for it to be located in the center of the pyrite crystals, in a similar way to how other metalloids are shown to incorporate into pyrite crystals⁵². This suggests that the organism and its surrounding environment played a significant role in creating a unique setting that allowed for the incorporation of As in a specific pattern into pyrite during early diagenesis.

Similar euhedral pyrite has been reported in black shales and Mn carbonate deposits in the adjacent Lastourville sub-basin in the Francevillian Group⁵¹. Morphological and isotopic investigations indicated that pyrite evolved over time, with pyrite crystals being smaller during early diagenesis and increasing in size and recrystallizing during later diagenesis and metamorphism⁵¹. This process created concentric zonations within pyrite crystals, with early diagenetic signatures concentrated at their centers, while later diagenetic and metamorphic conditions contributed to recrystallization and the deposition of pyrite with contrasting isotopic signatures around⁵¹. This model for pyrite precipitation further suggests that arsenic association with the center

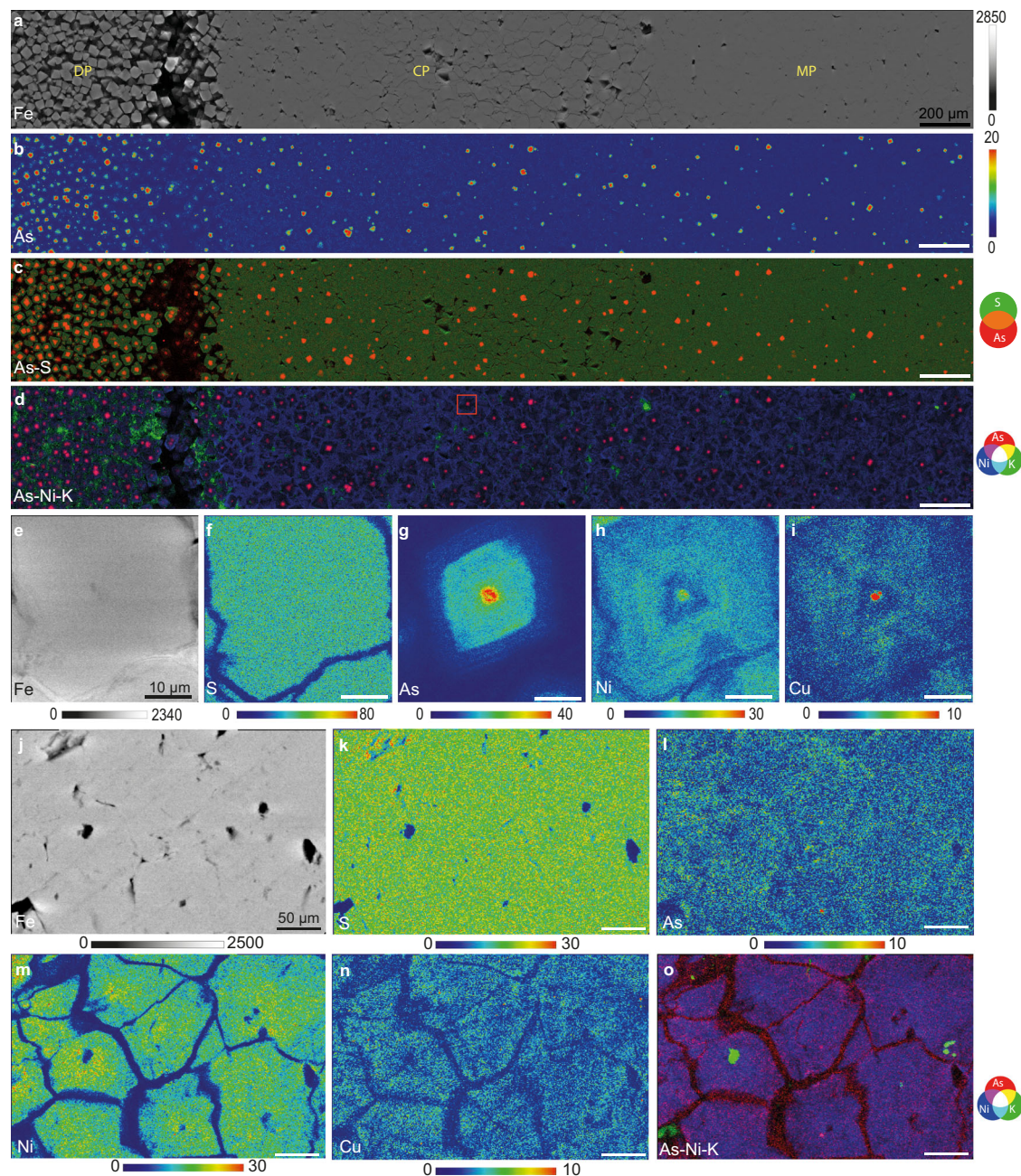


Fig. 4 | Arsenic intensity values and distribution in the investigated lobate macrofossils. **a** Nano-X-ray fluorescence (XRF) elemental map of iron (Fe) in a lobate fossil showing dispersed pyrite grains (DP) at the edge of the fossil, gradually decreasing porosity, increasing pyrite crystal size (coagulated pyrite, CP) and inward massive pyrite (MP). Nano-XRF elemental mapping of As (**b**) and As and S (As-S) (**c**) and concentric As distribution within pyrite grains. **d** Nano-XRF elemental mapping of As, Ni and K showing As zonation and association with Ni in pyrite grains found in a clay-rich matrix. Nano-XRF elemental mapping of Fe (**e**), S (**f**), As (**g**), Ni (**h**) and Cu (**i**) on one pyrite grain in a lobate specimen showing As nuclei in

association with Ni and Cu. Nano-XRF elemental mapping of Fe (**j**) and S (**k**) in an abiotic concretion within massive pyrite grains. **l** Nano-XRF elemental mapping of As illustrating diffuse distribution within pyrite, unlike in the case of biotic pyrite. Nano-XRF elemental mapping of Ni (**m**) and Cu (**n**) illustrating a homogeneous distribution pattern inside a pyrite grain. **o** Nano-XRF elemental mapping of As, Ni and K showing As enrichment at the border of abiotic pyrite grains, Ni inside the grains and K in peripheral clays. Pixel size **a–d** is 1 μm , **e–o** 150 nm. Dwell time: 20 ms/pixel.

of pyrite nuclei is of early diagenetic origin, even though the studied material was later subjected to weathering.

Interestingly, As-bearing pyrite is found in diverse environmental settings, playing a significant role as a primary sink for this toxic metalloid^{60,61}. One of the most common mineralogical forms of As is arsenopyrite (FeAsS⁶²), an As sulfide that typically forms through magmatic, metamorphic, and hydrothermal processes and rarely under sedimentary conditions, such as those under which these

complex specimens were replicated in pyrite. Our samples from the FB2b unit are neither metamorphosed nor associated with magmatic and hydrothermal processes. More importantly, As in arsenopyrite typically displays a homogeneous distribution throughout the crystals (Fig. 6e–h), unlike the patterns observed in the Francevillian macrofossils. Moreover, the As-bearing pyrite in these fossils is distinct from the patterns observed in standard pyrite Sun and pyrite Flower, or secondary pyrite observed in some pyritized ammonites (Fig. 6i–t).

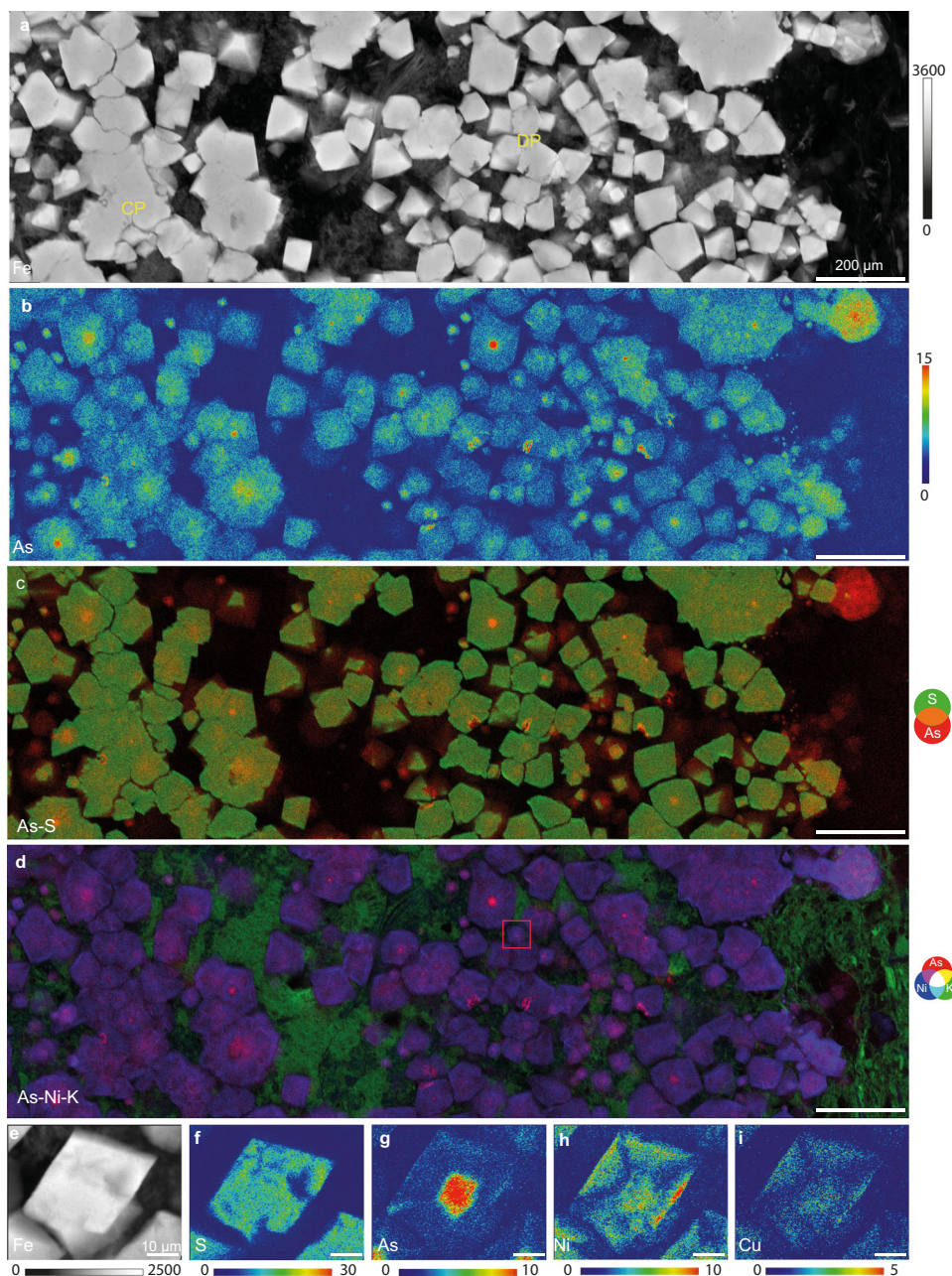


Fig. 5 | Arsenic intensity values and distribution in investigated tubular fossils. **a** Nano-X-ray fluorescence (XRF) elemental map of Fe in a tubular fossil showing dispersed pyrite grains (DP) and coagulated pyrite. Nano-XRF elemental mapping of As (**b**) and As and S (As-S) (**c**) showing a concentric As distribution within pyrite grains. **d** Nano-XRF elemental mapping of As, Ni, and K showing As zonation and

association with Ni in pyrite grains found in a clay-rich matrix. Nano-XRF elemental mapping of Fe (**e**), S (**f**), As (**g**), Ni (**h**), and Cu (**i**) on one pyrite grain in a lobate specimen showing As nuclei in association with Ni and Cu. Pixel size: **a–d** is 1 μm , **e–i** 150 nm. Dwell time: 20 ms/pixel.

This is corroborated by preliminary X-ray absorption near edge structure (XANES) analyses, performed in the As-rich core of some chosen pyrite crystals, revealing that As incorporated in the investigated Gabonese macrofossils occurs in the As^{3+} oxidation state in association with sulfides (e.g. As_2S_3) (Fig. 7a–e), contrasting with an oxidation state of As^{+5} typical of arsenopyrite (FeAsS), found in the chosen points of late diagenetic abiogenic concretions (Fig. 7f, g). These observations provide further evidence that distinct biogeochemical processes enriched As in the fossil structures and pyrite concretions.

Source of As enrichment in the macrofossils

Despite an As enrichment factor (EF) of <3 indicating low As concentrations in the Francevillan fossiliferous FB2b interval (Fig. 1f,

Table S1), As is predominantly concentrated within the fossils and mostly absent or extremely low levels in the rock matrix (Figs. 1f, 3b, S9). One possible explanation of these observations is that (i) most of the environmental As were attracted to the organic remains during early diagenesis and passively deposited in the pyrite crystals through chemical and physical processes, thereby quantitatively removing As from the rock matrix. Another scenario involves (ii) microbial incorporation of As into the pyrite crystals by storing it within their cells and, by some interactive process, concentrating it in the fossil specimens during pyritization. A third explanation is that (iii) As was systematically stored within the living organism during their lifetime through the process of bioaccumulation, with their dead remains acting as a key source of As during pyrite deposition.

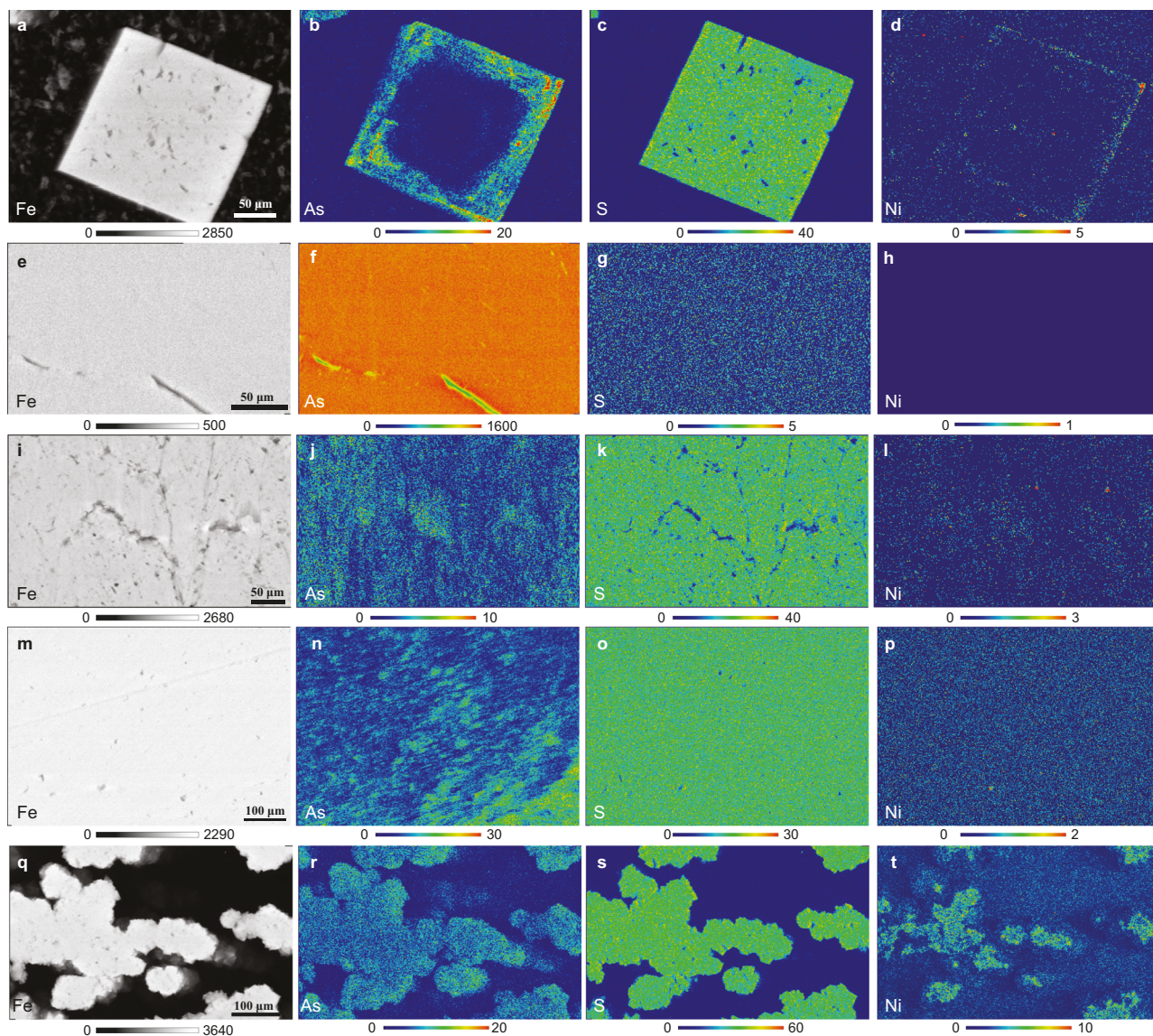


Fig. 6 | Arsenic repartitioning in abiotic specimens. Nano-XRF elemental mapping showing repartition of Fe, As, S, and Ni in **a–d** hydrothermal pyrite, **e–h** arsenopyrite, **i–l** Pyrite Sun, **m–p** Pyrite Flower, and **q–t** secondary pyrite in ammonite. Pixel size: 1 μm , dwell time: 20 ms/pixel.

The first scenario could have occurred, especially since organic matter binds metalloids during decay, resulting in metalloids accelerating the rate of pyrite nucleation and deposition at ambient temperatures⁵². However, this has only been observed so far for abiotic pyrite precipitation and never for biotic pyritization⁵². Moreover, it is inconceivable that all As in the environment would have been bound and concentrated in decaying biomass only a few centimeters in size. Importantly, the passive incorporation of environmental As into biogenic pyrite would likely result in a more homogenous association between both As and pyrite as it is observed in some stromatolite laminations from the 3.48 billion-year-old Dresser Formation (Pilbara Craton, Australia)⁶³. Thus, the As-rich core of the early diagenetic pyrite grains in the macrofossils suggests a pronounced biogenic control on the incorporation of As during pyrite nucleation. This could be due to either the association with microbial activity, for example, sulfate-reducing microorganisms, or the reflection of an intrinsic biochemical property of the decaying organism itself.

It is unlikely that the sulfate-reducing microorganisms involved in the fossilization process were the source of As, even though some bacteria can store As efficiently^{1,64}. Sulfate-reducing bacteria are highly

effective natural As decontaminating agents, as they reduce environmental As concentration by incorporating it into pyrite crystals^{65–67}. However, sulfate-reducing microbes are not known to store As in their bodies for prolonged durations, with their role often limited to moving As from their surrounding environment into pyrite^{65–67}. This process leads to the reduction of soluble As concentrations in the environment, as observed in As-contaminated soils and evidenced by the fossil record. For instance, As can be found associated with pyritized microbial mats^{37,63}. However, its presence is limited to the organic material surrounding microbial cells, forming the extracellular polymeric substance (EPS), and is not observed inside fossilized bacterial cells^{10,68,69}. In other words, despite the tolerance of sulfate-reducers to As and the possibility of them being able to integrate this element into their metabolism, these microbes were unlikely the source of As in the case of the complex specimen investigated in this study. If this were the case, a uniform distribution of As within the pyrite crystals would be expected, as the same sulfate-reducing microbes should in principle be responsible for pyrite nucleation and growth during early diagenesis⁷⁰. In this sense, sulfate reducers facilitated As precipitation into pyrite, but were not the source of As.

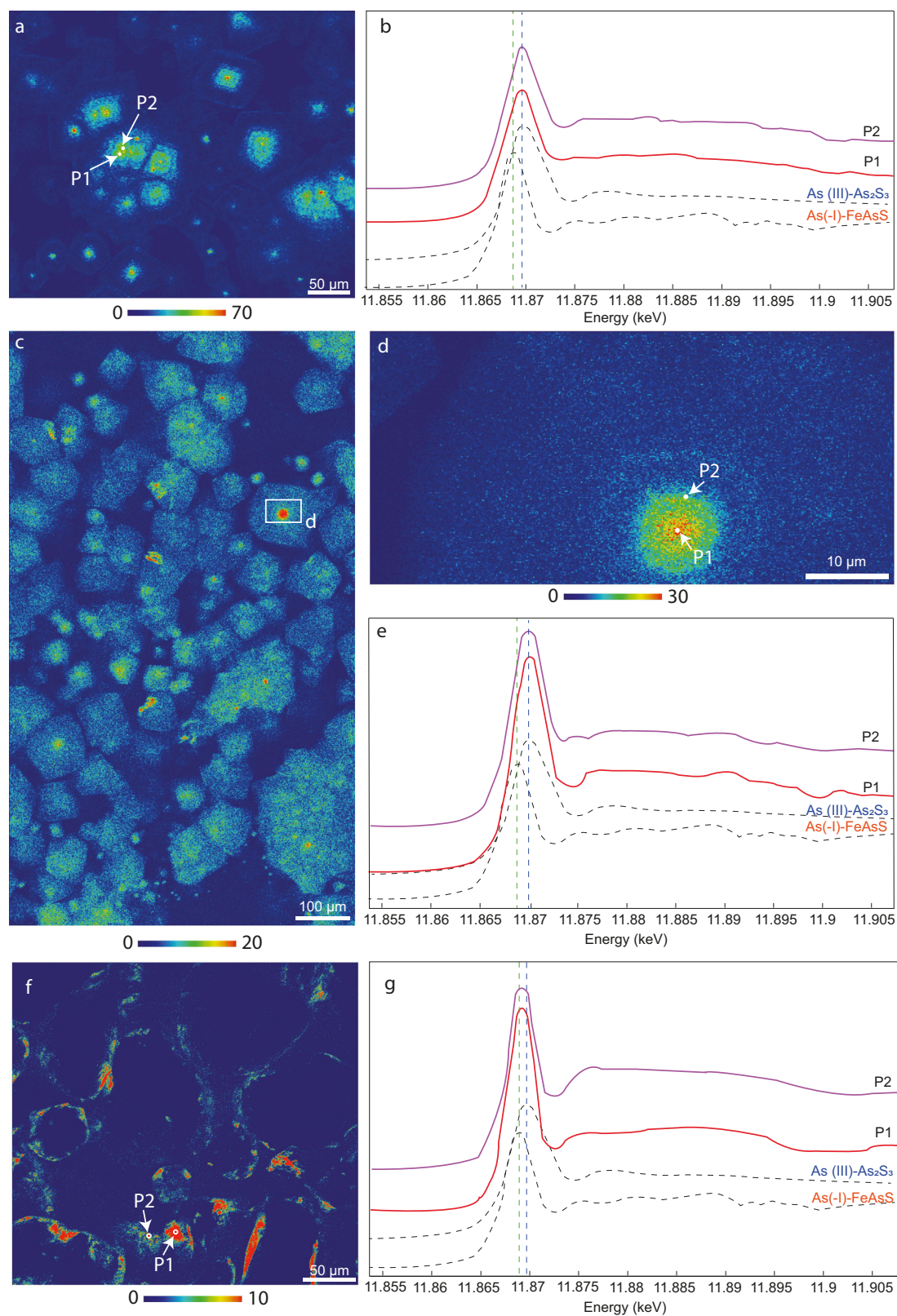


Fig. 7 | Arsenic nano-XANES in some chosen points in fossil specimens and abiotic concretions. **a** P1 and P2 were selected within pyrite in a lobate specimen. **b** Arsenic XANES spectra measured in P1 and P2 compared to As₂S₃ and FeAsS reference XANES spectra. **c**, **d**, P1 and P2 were selected within pyrite in a tubular

macrofossil specimen. **e** As XANES spectra measured in P1 and P2 compared with As₂S₃ and FeAsS reference XANES spectra. **f** P1 and P2 chosen in an abiotic concretion specimen. **g** As XANES spectra measured in P1 and P2 compared with As₂S₃ and FeAsS reference XANES spectra.

Thus, the third scenario is the most plausible. In other words, patterns of As association in early diagenetic pyrite point to bioaccumulation of As—a process by which certain toxins and chemicals accumulate in an organism's body over time because they are absorbed much faster than they are broken down or excreted. The low As concentration in the bulk rock, together with the absence of comparable As enrichment trends in the pyrite concretions as in the fossils, coupled with similar enrichment patterns in the Phanerozoic macrofossils, point to a process that systematically bioaccumulated trace amounts of As in the living biomass. These observations hint at the strong possibility that As enriched in the macrofossil pyrite grains is the consequence of oxidation of bioaccumulated As-rich organic residues during early diagenesis by sulfate-reducing microbes.

Arsenic detoxification as an adaptive evolutionary tool in the Francevillian biota

Arsenic is notoriously toxic to all living organisms because arsenite deactivates proteins and arsenate interferes with phosphate metabolism because of their closely shared physicochemical properties, making it a monumental challenge for cells to discriminate between phosphate and arsenate¹⁵. For example, the competition between arsenate and phosphate to enter cells through phosphate transporters implies high environmental arsenate to phosphate ratios starve cells of phosphate, and has led to the development of energetically costly molecular mechanisms to discriminate between the two¹⁵. Once inside the cell, arsenate can inhibit the activity of adenosine triphosphate (ATP), nucleic acids involved in the production and transfer of hereditary information and protein synthesis, phospholipids that form cell membranes and various reactions involving phosphate transfer that generate biomolecules, for example, by arsenolysis during glycolysis⁷¹. When arsenate replaces phosphate, it forms an unstable anhydride⁷². Arsenic levels in the studied material were low, suggesting that while the As/P ratios remained relatively stable across the succession (Fig. 1e), it potentially promoted unique long-term As enrichment inside the macrofossils (Fig. 3b). These observations suggest that arsenate entered biomass principally by passive transportation across phosphate transporters and that high-affinity discrimination of phosphate was likely not prominent in these organisms.

Living organisms cope with excessive As concentrations by detoxifying and extruding As from biomass using efflux pumps²². For example, cyanobacteria circumvent high environmental arsenate-to-phosphate ratios by adapting specific high-affinity phosphate uptake channeling as a detoxification response⁷³. Like most microbes, they possess the bacterial-specific *ArsC* gene that catalyzes the conversion of As⁵⁺ to As³⁺, followed by extrusion without getting rid of the cell's phosphate⁷⁴. Many phytoplankton (e.g., *Prochlorococcus*) add methyl groups to remove it from water⁷⁵. Modern eukaryotes equally reduce As⁵⁺ to As³⁺ using As⁵⁺ reducing enzymes, an analog of the prokaryotic *ArsC* gene known as *Acr2p*^{66,73}, before extrusion from the cytosol. Despite having evolved by convergent evolution and therefore not genetically related, *ArsC* and *Acr2p* enzymes derive their reducing power from glutaredoxin and reduced glutathione, pointing to the significant impact As stress has had on biological evolution across the tree of life. In the absence of efflux pumps As is compartmentalized and sequestered within internal vacuoles and vesicles in eukaryotes¹⁹.

The co-occurrence of Cu and Ni with As in pyrite with the macrofossils (Figs. 4g–i, 5g–i & Fig. S2) suggests additional sequestration of these micronutrients, which, while essential, are toxic at high concentrations⁷⁶. Copper could be sequestered internally and externally due to its high absorption capacity^{77,78}. Nickel, when in excess, is chelated (i.e., binding of Ni ions with ligands) and transported into vacuoles^{79,80}. For example, the major coupling of hydrothermal activity with anoxia, sea level rise and extreme input of toxic metals, including As in sediments located above the macrofossil-hosting beds, ultimately led to their extinction (Fig. 1a; Supplementary Material).

Arsenic bioaccumulation and its evolutionary implications for the Francevillian biota

The complex macrofossils studied here thrived in a low As environment, probably due to a low As content in the continental rocks that formed the principal source of As to the Francevillian basin (Fig. 1f). As stated previously, in the oxygenated seawater in which these organisms lived, arsenate was likely the dominant form of As, as observed in modern oxygenated seawater (Fig. 8a). In these conditions, due to its strong physical and chemical similarities with phosphate, As⁵⁺ passively entered biomass through phosphate transporters, the primary pathway for its uptake in modern living organisms (Fig. 8b). Once inside the cells, arsenate was enzymatically converted into arsenite and extruded or compartmentalized in intracellular vacuoles or vesicles (Fig. 8c, d). The importance of As storage by some metazoans as an As detoxification mechanism is demonstrated in the marine sponge *Theonella swinhoei*, reputed for accumulating high levels of toxic metals within their bodies^{81,82}. Notably, sponges constitute some of Earth's earliest known multicellular eukaryotes, with *Theonella swinhoei* recruiting symbiotic bacteria within their bodies to store As within intracellular vesicles⁸², in the absence of an ability to detoxify As by extrusion. A variety of sponges studied in the Atlantic Ocean and Mediterranean Sea store As mainly in the form of arsenobetaine (AsB) and low amounts of dimethylarsinic acid or DM⁸³.

Like modern sponges, the Francevillian specimens may represent some of the Earth's earliest filter feeders. This lifestyle, which exposed them to metal(loid)s, potentially drove the need for adaptive detoxification by bioaccumulation. For instance, while immediate As extrusion may be essential in avoiding acute toxicity, the low-level exposure to As like in our samples, would likely only become problematic after prolonged exposure. This would allow bioaccumulation over an extended lifespan without causing serious injury. Arsenobetaine, an organic As compound prevalent in up to 80% of all marine organisms^{22,84}, compared to most organo-As compounds, is relatively non-toxic to most complex eukaryotes⁸⁵. In marine organisms, arsenobetaine is thought to also function as an osmolyte, regulating osmotic pressure to maintain cellular balance under environmental stress²². For instance, the release of osmolytes and water restores a cell's volume during swelling. Thus, organisms living in low-As, high-salinity marine environments and capable of storing arsenobetaine within their bodies as a detoxification mechanism and as an osmolyte likely faced a lesser evolutionary pressure to develop or acquire energy-intensive As-extrusion mechanisms. Moreover, in this low As environment, intracellular sequestration would have been sufficient to minimize the toxic effects of As³⁺ on proteins and the interference of As⁵⁺ with phosphate metabolism. Over time, this process would have resulted in the gradual bioaccumulation of As within the living Francevillian biomass, offering a potential mechanism for the unique enrichment of As in the macrofossils. Notably, such enrichment was not found in the pyritized concretions, despite being formed in the same low As-containing environment in which the macrofossils were preserved.

Following the death of these organisms, As³⁺ was released (Fig. 8e) and incorporated into pyrite at the sites of nucleation during microbial sulfate reduction of As³⁺-rich organic residues and vesicles (Fig. 8f). The oxidation state of As in the macrofossils (Fig. 7) further points to the formation of As³⁺-rich sulfides under post-mortem sulfate-reducing bacteria conditions. The formation of orpiment (As₂S₃) has been documented following As(V) bioreduction in a sulfide-rich environment⁸⁶. For example, microorganisms oxidize As-rich organic molecules, such as arsenobetaine and methylated arsenicals, to obtain energy gains⁶⁹. Because As was limited in the localized environment, its incorporation into the growing pyrite crystals, therefore, decreased further from the nucleation sites (Fig. 8e, f).

This pyritization model offers the most parsimonious explanation of the observed As distribution patterns and is consistent with

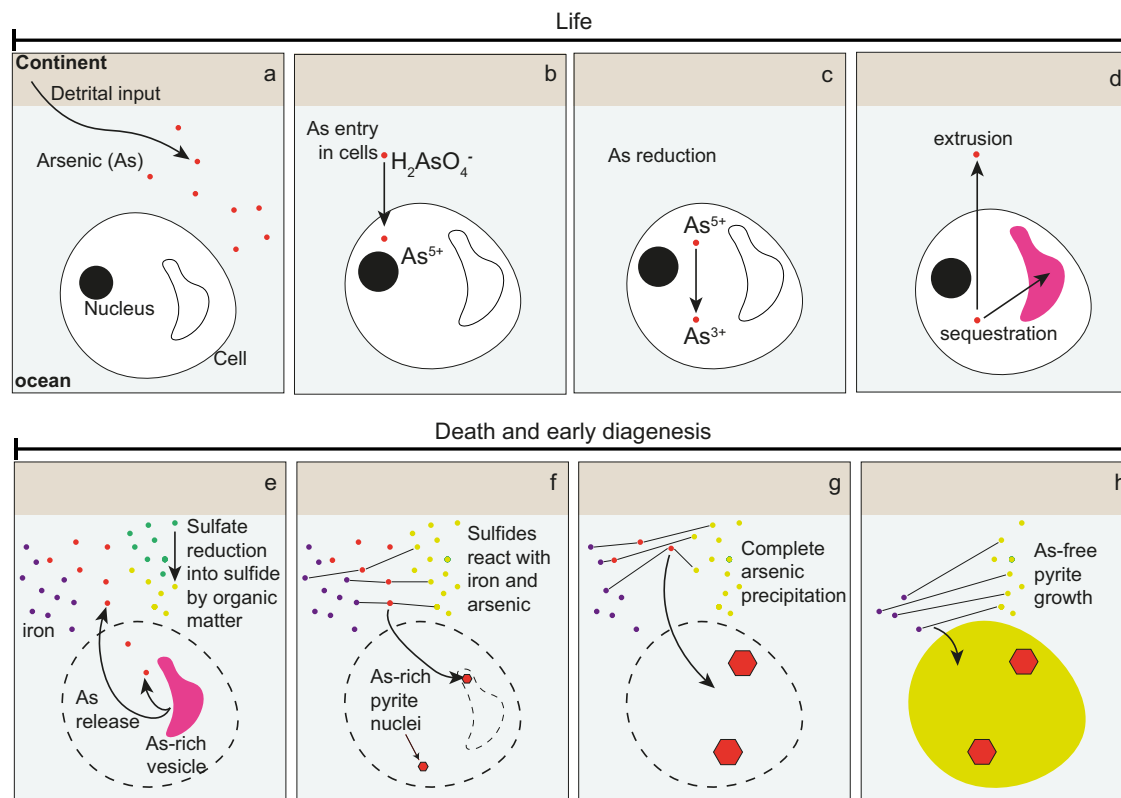


Fig. 8 | Conceptual model for the biological formation of fossilized As-rich pyrite nuclei. **a** Oxidized As—arsenate or As^{5+} (red dots) is released into the ocean by the chemical and oxidative weathering of the continental crust. **b** During life, As enters the cell, and is detoxified first by reduction to As^{3+} (**c**) then extruded by cell membrane transporters or sequestered in intracellular compartments (**d**). **e** After death and burial, As is released from intracellular bodies into a localized reduced

environment rich in iron (purple dots) where sulfate (green dots) is reduced to sulfides (yellow dots). **f** Pyrite is formed by microbial sulfate reduction with As acting as a catalyzer of pyrite nucleation. **g** Arsenic is rapidly consumed in low environmental concentrations. **h** Pyrite growth led to As depletion away from the core.

previous models where decaying carcasses influence pyrite formation^{87–89}. In summary, As incorporation into pyrite associated with the macrofossils occurred during early diagenesis, specifically during pyrite nucleation. At this stage, As was scarce in the surrounding environment and was primarily sourced from decaying biomass. This indicates that these organisms stored large quantities of As in their bodies during their lifetime. Our observations are further supported by comparable observations of As preservations in Phanerozoic metazoans (see Supplementary Information for more details).

This study explores how Earth's primitive eukaryotes from the 2.1 Ga Francevillian sub-basin, managed environmental exposure to As, a notorious toxin to all life forms. The results suggest that these ancient organisms sequestered As within their bodies as a detoxification strategy. This hypothesis is supported by the significant As enrichment in fossils despite low environmental levels, indicating progressive bioaccumulation. The unique presence of arsenic nuclei in pyrite—indicative of arsenic-catalyzed post-mortem pyrite formation under early diagenetic-microbial sulfate reduction conditions, specific to these organisms—coupled with a somewhat similar enrichment pattern in certain pyritized Phanerozoic eumetazoans, supports the biogenic origin of the Francevillian fossils. These insights not only reinforce their biological nature but also offer a tool for detecting ancient life, especially in cases where organic material has been lost or replaced by authigenic minerals.

Methods

Hundreds of samples were collected from the FB2b black shales including pyritized lobate, elongate and tubular fossils, as well as

abiotic concretions all found in the same location in the Moulendé quarry³¹. Selected polished sections were carbon-coated and examined using JEOL JSM IT500 Scanning Electron Microscope at the University of Poitiers, France (HT = 15 KV, WD = 11 mm, PC = 1 nA). The scanning electron microscopy (SEM) instrument was equipped with secondary electron (SE) and backscatter electron (BSE) detectors.

Whole-rock geochemical analyses of major and trace elements were also performed on 316 samples⁹⁰ representative of the different stratigraphic units of the Francevillian (Supplementary material). Each sample was powdered using an agate mortar and approximately 1 g was fused with lithium metaborate (LiBO_2) and dissolved in dilute nitric acid (HNO_3). Major element (Si, Al, Fe, Mn, Mg, Ca, Na, K, Ti, and P) concentrations were measured by inductively coupled plasma optical emission spectrometry (ICP-OES), while As content was analyzed by inductively coupled plasma mass spectrometry (ICP-MS) at the Service d'Analyse des Roches et Minéraux (SARM) of the Center de Recherches Pétrographiques et Géochimiques (CRPG), Nancy, France. Some of these analyses in this study were previously treated and compiled^{33,35,37,91}. The depth trend does not reflect the actual placement in the stratigraphy.

The enrichment factor (EF) of As (UCC:1.5^{92}) relative to the average shale was used to assess whether As was enriched or depleted. The EF is considered detectable and substantial when greater than 3 and 10, respectively⁹³. The EF was calculated as $[(\text{As}/\text{Al})_{\text{sample}} / (\text{As}/\text{Al})_{\text{average shale}}]$. The intensity of weathering in the source area can be determined with the chemical index of alteration ($\text{CIA} = \text{molar}[\text{Al}_2\text{O}_3] / (\text{Al}_2\text{O}_3 + \text{CaO}^* + \text{Na}_2\text{O} + \text{K}_2\text{O}) \times 100$) where CaO^* is the CaO content only in the silicates, and measures the degree of feldspar conversion to clays⁹⁴. CaO is first corrected for that residing

in apatite using P_2O_5 data ($CaO' = CaO - 10/3 \times P_2O_5$) and if CaO' is superior to Na_2O , then the final CaO^* value is set to equal to Na_2O . If the value is inferior to the value of Na_2O , then the final CaO^* is equal to CaO' value. To correct CIA values for K metasomatism, the following formulas were used⁹⁵:

$$m = K_2O / (Al_2O_3 + CaO^* + Na_2O + K_2O) \text{ for archean TTG sample} \quad (1)$$

$$K_2O_{corr} = \text{molar} \left[m \times (CaO^* + Na_2O) \right] / (1 - m) \quad (2)$$

$$CIA_{corr} = \text{molar } Al_2O_3 / (Al_2O_3 + CaO^* + Na_2O + K_2O_{corr}) \quad (3)$$

Fifteen polished cross-sections (four lobates, two tubulars and, two concretions from the Francevillian basin of Gabon, one ammonite from Les Deux-Sèvres, France, one crab MNHN.F.R03360 and, one shrimp MNHN.F.A.98018 from the National Museum of Natural History of Paris (MNHN), one arsenopyrite from Panasqueira mine, Portugal, one pyrite Sun from USA and one pyrite Flower from Germany acquired from the Swedish Museum of Natural History, one hydrothermal pyrite from Le Mans, France) and two sections stored in the collection of the Natural History Museum Vienna (one Burgess shale Marella and one echinoderm) were chosen for scanning X-ray fluorescence analysis. The SR nano-XRF and nano-XANES measurements were performed in multi-bunch beam operation mode on several areas within the studied samples at the NANOSCOPIUM hard X-ray nanoprobe beamline⁹⁶, Synchrotron SOLEIL, France. A Si(111) double-crystal fixed-exit monochromator was used for obtaining a monochromatic X-ray beam of 12 keV, just above the electron binding energy of the As K-edge. An achromatic nano-focusing Kirkpatrick-Baez (KB) mirror pair (JTEC) has been used for creating a 150 nm (FWHM) sized nano-beam at the sample position. Two silicon drift diode detectors (SDD, VITUS H50, KETEK GmbH), situated symmetrically around the sample, were used for the measurements. The X-ray flux in the nano-beam has been adjusted in the $[5 \times 10^8 - 5 \times 10^9]$ photons/s range for each sample to keep the XRF detector's deadtime below 25% in order to optimize the quality of the XRF spectra. All scanning imaging was performed by using continuous sample scanning (FLYSCAN) developed at Synchrotron Soleil. The pixel size of the elemental distribution maps was in the 1 for coarse scans of mm-sized sample areas, except for the Phanerozoic fossils measured with (5 μ m pixel size) shown in Figs. S5b–e, l–q, and in the 150–300 nm range for deca- μ m² scanned zones using 20–50 ms/pixel dwell times. An 8 μ m-thick silicon diode situated upstream of the KB mirrors was used as an intensity monitor to correct for the variation of the incident flux on the samples. In each measurement point (i.e., in each pixel for XRF imaging or in each energy step for XANES) we have collected full XRF spectra. The sum spectra of the analyzed sample areas have been fitted with the PyMCA software. The distribution maps of the elements identified from the sum-XRF-spectra were created either by PyMCA or by a homemade MATLAB code, including corrections for deadtime, measurement time, beam intensity, and eventual spectral overlapping. Several areas have been studied for each sample. From the reconstructed elemental maps, the distributions of Fe, S, As, K, Ni, Cu, and Ca were relevant for the recent study.

Nano X-ray absorption near edge structure spectroscopy (nano-XANES) has been performed in the very same measurement geometry as described above in nine As-rich pyrite nuclei in the macrofossils and three As hotspots in the pyritized concretions. The incident X-ray beam energy was scanned across the 11.825–11.910 keV energy range in 0.5 eV increments, and the data was collected in X-ray fluorescence (XRF) mode. The measurement time at each energy point was 1 s. Each XANES measurement in each measured sample point has been performed at least 3 times. These repetition scans showed no detectable

photo-oxidation/photoreduction-related alteration in the XANES spectra.

The trace element concentrations of 100 pyrite grains (29 in tubular, 51 in lobate, and 20 concretions) from ten polished slabs of pyritized macrofossils and concretions specimens (three tubular, five lobate and two concretions) were measured by LA-ICP-MS using an Analyte G2 Excimer laser ablation system (193 nm), coupled to a quadrupole Agilent 7900 ICP-MS at the Institut de Physique du Globe de Paris, Université Paris Cité. Pyrite grains were ablated using a laser spot of 20 μ m diameter to avoid the analysis of matrix material. LA-ICP-MS analyses consisted of 60 s period to measure the background (gas blank) and 30 s period for analysis. A total of eight runs were carried out in July 2018. No correction was applied for variations in the Fe internal standard. Each sample was bracketed by three analyses of MASS-1 standard. The following isotopes were monitored: ⁵⁵Mn, ⁵⁷Fe, ⁵⁹Co, ⁶⁰Ni, ⁶³Cu, ⁶⁶Zn, ⁷⁵As, ⁸²Se, ⁹⁵Mo, ¹⁰⁷Ag, ¹⁰⁹Ag, ¹¹¹Cd, ¹²¹Sb, ¹⁹⁷Au, ²⁰⁸Pb, ²⁰⁹Bi. The element ratios were calculated for each specimen, and a geometric mean was established. ANOVA test was performed on these data to study the significance of As concentration variance using PAST software.

Raw counts were processed using IOLITE v3.65 software with MASS-1 standard⁹⁷ used for calibrating the elements and Fe as an internal standard. Time-resolved spectra were checked for accuracy by removing mixed signals in the analyzed volumes. Detection limits (DL) for each element per run were calculated as follows: DL = meanblank + (3 * standard deviation) blank. When elemental concentrations were lower than the DL values were discarded. ANOVA *F*-statistic test was made to study the significance of As concentration variations between different types of specimens.

Data availability

Information materials are available in the main text or the Supplementary Materials. Source data are provided with this paper.

References

- Rosen, B. P. Biochemistry of arsenic detoxification. *FEBS Lett.* **529**, 86–92 (2002).
- Pongratz, R. Arsenic speciation in environmental samples of contaminated soil. *Sci. Total Environ.* **224**, 133–141 (1998).
- Campbell, K. M. & Nordstrom, D. K. Arsenic speciation and sorption in natural environments. *Rev. Mineral. Geochem.* **79**, 185–216 (2014).
- Hughes, M. F. et al. Tissue dosimetry, metabolism and excretion of pentavalent and trivalent dimethylated arsenic in mice after oral administration. *Toxicol. Appl. Pharmacol.* **227**, 26–35 (2008).
- Oremland, R. S. & Stolz, J. F. The Ecology of Arsenic. *Science* **300**, 939–944 (2003).
- Sforza, M. C., Van Zuilen, M. A. & Philippot, P. Structural characterization by Raman hyperspectral mapping of organic carbon in the 3.46 billion-year-old Apex chert, Western Australia. *Geochim. Cosmochim. Acta* **124**, 18–33 (2014).
- Kulp, T. R. et al. Arsenic(III) fuels anoxygenic photosynthesis in hot spring biofilms from Mono Lake, California. *Science* **321**, 967–970 (2008).
- Visscher, P. T. et al. Modern arsenotrophic microbial mats provide an analogue for life in the anoxic Archean. *Commun. Earth Environ.* **1**, 24 (2020).
- Chraiki, I. et al. Blooming of a microbial community in an Ediacaran extreme volcanic lake system. *Sci. Rep.* **13**, 9080 (2023).
- Chraiki, I. et al. A 571 million-year-old alkaline volcanic lake photosynthesizing microbial community, the Anti-atlas, Morocco. *Geobiology* **19**, 105–124 (2021).
- Saunders, J. K., Fuchsman, C. A., McKay, C. & Rocap, G. Complete arsenic-based respiratory cycle in the marine microbial communities of pelagic oxygen-deficient zones. *Proc. Natl Acad. Sci. USA* **116**, 9925–9930 (2019).

12. Sancho-Tomás, M. et al. Geochemical evidence for arsenic cycling in living microbialites of a high altitude Andean Lake (Laguna Diamante, Argentina). *Chem. Geol.* **549**, 119681 (2020).
13. Oremland, R. S., Stolz, J. F. & Hollibaugh, J. T. The microbial arsenic cycle in Mono Lake, California. *FEMS Microbiol. Ecol.* **48**, 15–27 (2004).
14. Chi Fru et al. Arsenic and high affinity phosphate uptake gene distribution in shallow submarine hydrothermal sediments. *Bio-geochemistry* **141**, 41–62 (2018).
15. Elias, M. et al. The molecular basis of phosphate discrimination in arsenate-rich environments. *Nature* **491**, 134–137 (2012).
16. Ben Fekih, I. et al. Distribution of arsenic resistance genes in prokaryotes. *Front. Microbiol.* **9**, 2473 (2018).
17. Verbruggen, N., Hermans, C. & Schat, H. Mechanisms to cope with arsenic or cadmium excess in plants. *Curr. Opin. Plant Biol.* **12**, 364–372 (2009).
18. Vahter, M. Species differences in the metabolism of arsenic compounds. *Appl. Organo Chem.* **8**, 175–182 (1994).
19. Ghosh, M., Shen, J. & Rosen, B. P. Pathways of As(III) detoxification in *Saccharomyces cerevisiae*. *Proc. Natl Acad. Sci. USA* **96**, 5001–5006 (1999).
20. Lyons, T. W. Co-evolution of early Earth environments and microbial life. *Nat. Rev. Microbiol.* **22**, 572–586 (2024).
21. Poulton, S. W. et al. A 200-million-year delay in permanent atmospheric oxygenation. *Nature* **592**, 232–236 (2021).
22. Chen, S.-C. et al. The Great Oxidation Event expanded the genetic repertoire of arsenic metabolism and cycling. *Proc. Natl Acad. Sci. USA* **117**, 10414–10421 (2020).
23. Chi Fru et al. The rise of oxygen-driven arsenic cycling at ca. 2.48 Ga. *Geology* **47**, 243–246 (2019).
24. Garbinski, L. D., Rosen, B. P. & Chen, J. Pathways of arsenic uptake and efflux. *Environ. Int.* **126**, 585–597 (2019).
25. Ikouanga, J. N. et al. The first application of Re–Os dating on Paleoproterozoic Francevillian sediments (Gabon). *C. R. Géosci.* **356**, 57–66 (2024).
26. Anderson, R. P., Tarhan, L. G., Cummings, K. E., Planavsky, N. J. & Bjørnerud, M. Macroscopic structures in the 1.1 Ga continental Copper Harbor formation: concretions or fossils? *PALAIOS* **31**, 327–338 (2016).
27. Fakhraee, M. et al. Earth's surface oxygenation and the rise of eukaryotic life: relationships to the Lomagundi positive carbon isotope excursion revisited. *Earth* **240**, 104398 (2023).
28. El Albani, A. et al. Large colonial organisms with coordinated growth in oxygenated environments 2.1 Gyr ago. *Nature* **466**, 100–104 (2010).
29. El Albani, A. et al. The 2.1 Ga Old Francevillian Biota: biogenicity, taphonomy and biodiversity. *PLoS ONE* **9**, e99438 (2014).
30. El Albani, A. et al. Organism motility in an oxygenated shallow-marine environment 2.1 billion years ago. *Proc. Natl Acad. Sci. USA* **116**, 3431–3436 (2019).
31. Ikouanga, J. N. et al. Taphonomy of early life (2.1 Ga) in the Francevillian basin (Gabon): role of organic mineral interactions. *Precambrian Res.* **395**, 107155 (2023).
32. Ossa Ossa, F. et al. Zinc enrichment and isotopic fractionation in a marine habitat of the c. 2.1 Ga Francevillian Group: A signature of zinc utilization by eukaryotes? *Earth Planet. Sci. Lett.* **611**, 118147 (2023).
33. Aubineau, J. et al. Unusual microbial mat-related structural diversity 2.1 billion years ago and implications for the Francevillian biota. *Geobiology* **16**, 476–497 (2018).
34. El Albani, A. et al. A search for life in Palaeoproterozoic marine sediments using Zn isotopes and geochemistry. *Earth Planet. Sci. Lett.* **612**, 118169 (2023).
35. Chi Fru, E. et al. Hydrothermal seawater eutrophication triggered local microbiological experimentation in the 2100 Ma Paleoproterozoic Francevillian sub-basin. *Precambrian Res.* **409**, 107453 (2024).
36. Canfield, D. E. et al. Oxygen dynamics in the aftermath of the Great Oxidation of Earth's atmosphere. *Proc. Natl Acad. Sci. USA* **110**, 16736–16741 (2013).
37. Aubineau, J. et al. Trace element perspective into the ca. 2.1-billion-year-old shallow-marine microbial mats from the Francevillian Group, Gabon. *Chem. Geol.* **543**, 119620 (2020).
38. Boström, K. Submarine volcanism as a source for iron. *Earth Planet. Sci. Lett.* **9**, 348–354 (1970).
39. Pecoits, E. et al. Petrography and geochemistry of the Dales Gorge banded iron formation: paragenetic sequence, source and implications for palaeo-ocean chemistry. *Precambrian Res.* **172**, 163–187 (2009).
40. Tribovillard, N. Arsenic in marine sediments: how robust a redox proxy? *Palaeogeogr. Palaeoclimatol. Palaeoecol.* **550**, 109745 (2020).
41. Tribovillard, N. Conjugated enrichments in arsenic and antimony in marine deposits used as paleoenvironmental proxies: preliminary results. *BSGF Earth Sci. Bull.* **192**, 39 (2021).
42. Ossa Ossa, F. et al. Two-step deoxygenation at the end of the Paleoproterozoic Lomagundi Event. *Earth Planet. Sci. Lett.* **486**, 70–83 (2018).
43. Chi Fru, E. et al. Arsenic stress after the Proterozoic glaciations. *Sci. Rep.* **5**, 17789 (2015).
44. Cullen, W. R. & Reimer, K. J. Arsenic speciation in the environment. *Am. Chem. Soc.* **89**, 713–764 (1989).
45. Smedley, P. L. & Kinniburgh, D. G. A review of the source, behaviour and distribution of arsenic in natural waters. *Appl. Geochem.* **17**, 517–568 (2002).
46. Dill, H. & Kemper, E. Crystallographic and chemical variations during pyritization in the upper Barremian and lower Aptian dark claystones from the Lower Saxonian Basin (NW Germany). *Sedimentology* **37**, 427–443 (1990).
47. Guy, B. M., Beukes, N. J. & Gutzmer, J. Paleoenvironmental controls on the texture and chemical composition of pyrite from non-conglomeratic sedimentary rocks of the Mesoarchean Witwatersrand Supergroup, South Africa. *South Afr. J. Geol.* **113**, 195–228 (2010).
48. Bajwah, Z. U., Seccombe, P. K. & Offler, R. Trace element distribution, Co:Ni ratios and genesis of the Big Cadia iron-copper deposit, New South Wales, Australia. *Mineral. Deposita* **22**, 292–300 (1987).
49. Gregory, D. D. et al. Trace element content of sedimentary pyrite in black shales. *Econ. Geol.* **110**, 1389–1410 (2015).
50. Thomas, H. V. et al. Pyrite and pyrrhotite textures and composition in sediments, laminated quartz veins, and reefs at Bendigo Gold Mine, Australia: Insights for Ore Genesis. *Econ. Geol.* **106**, 1–31 (2011).
51. Paiste, K. et al. Sulfur isotopes from the Paleoproterozoic Francevillian Basin record multigenerational pyrite formation, not depositional conditions. *Commun. Earth Environ.* **5**, 328 (2024).
52. Morin, G. et al. Nickel accelerates pyrite nucleation at ambient temperature. *Geochem. Persp. Lett.* <https://doi.org/10.7185/geochemlet.1738> (2017).
53. Jagt, J. W. M. Coeloma rupeliense (Crustacea, Decapoda, Brachyura) from the Bilzen Formation (Rupel Group, Lower Oligocene) in Northeast Belgium. *Bulletin de l'Institut Royal des Sciences Naturelles de Belgique, Sciences de la Terre.* **80**, 245–252 (2010).
54. Jauvion, C., Charbonnier, S. & Bernard, S. A new look at the shrimps (Crustacea, Decapoda, Penaeoidea) from the Middle Jurassic La Voulte-sur-Rhône Lagerstätte. *Geodiversitas* **39**, 705–716 (2017).
55. Large, R. R. et al. Gold and trace element zonation in pyrite using a laser imaging technique: implications for the timing of gold in orogenic and carlin-style sediment-hosted deposits. *Econ. Geol.* **104**, 635–668 (2009).

56. Large, R. R. et al. Trace element content of sedimentary pyrite as a new proxy for deep-time ocean–atmosphere evolution. *Earth Planet. Sci. Lett.* **389**, 209–220 (2014).
57. Kutzschbach, M. et al. Arsenic-poor fluids promote strong As partitioning into pyrite. *Geochim. Cosmochim. Acta* **376**, 37–53 (2024).
58. Genna, D. & Gaboury, D. Deciphering the hydrothermal evolution of a VMS system by LA-ICP-MS using trace elements in pyrite: an example from the Bracemac-McLeod Deposits, Abitibi, Canada, and implications for exploration. *Econ. Geol.* **110**, 2087–2108 (2015).
59. Steadman, J. A. et al. Pyrite trace element behavior in magmatic-hydrothermal environments: an LA-ICPMS imaging study. *Ore Geol. Rev.* **128**, 103878 (2021).
60. Le Pape, P. et al. Arsenic incorporation in pyrite at ambient temperature at both tetrahedral S²⁻ and octahedral Fe³⁺ sites: evidence from EXAFS–DFT analysis. *Environ. Sci. Technol.* **51**, 150–158 (2017).
61. Wells, J. D. & Mullens, T. E. Gold-bearing arsenian pyrite determined by microprobe analysis, Cortez and Carlin gold mines, Nevada. *Econ. Geol.* **68**, 187–201 (1973).
62. Ning, R. Y. Arsenic in Natural Waters. in *Water Encyclopedia* (eds Lehr, J. H. & Keeley, J.) 81–83 <https://doi.org/10.1002/047147844X.mw13> (Wiley, 2004).
63. Baumgartner, R. J. et al. Accumulation of transition metals and metalloids in sulfidized stromatolites of the 3.48 billion-year-old Dresser Formation, Pilbara Craton. *Precambrian Res.* **337**, 105534 (2020).
64. Yan, G. et al. Genetic mechanisms of arsenic detoxification and metabolism in bacteria. *Curr. Genet* **65**, 329–338 (2019).
65. Rittle, K. A., Drever, J. I. & Colberg, P. J. S. Precipitation of arsenic during bacterial sulfate reduction. *Geomicrobiol. J.* **13**, 1–11 (1995).
66. Macy, J. M., Santini, J. M., Pauling, B. V., O'Neill, A. H. & Sly, L. I. Two new arsenate/sulfate-reducing bacteria: mechanisms of arsenate reduction. *Arch. Microbiol.* **173**, 49–57 (2000).
67. Kirk, M. F. et al. Bacterial sulfate reduction limits natural arsenic contamination in groundwater. *Geology* **32**, 953 (2004).
68. Sancho-Tomás, M. et al. Distribution, redox state and (bio)geochemical implications of arsenic in present day microbialites of Laguna Brava, Salar de Atacama. *Chem. Geol.* **490**, 13–21 (2018).
69. Sforza, M. C. et al. Patterns of metal distribution in hypersaline microbialites during early diagenesis: implications for the fossil record. *Geobiology* **15**, 259–279 (2017).
70. Alam, R. & McPhedran, K. Applications of biological sulfate reduction for remediation of arsenic—a review. *Chemosphere* **222**, 932–944 (2019).
71. Hughes, M. F. Arsenic toxicity and potential mechanisms of action. *Toxicol. Lett.* **133**, 1–16 (2002).
72. Gresser, M. J. ADP-arsenate. Formation by submitochondrial particles under phosphorylating conditions. *J. Biol. Chem.* **256**, 5981–5983 (1981).
73. Mukhopadhyay, R., Rosen, B. P., Phung, L. T. & Silver, S. Microbial arsenic: from geocycles to genes and enzymes. *FEMS Microbiol. Rev.* **26**, 311–325 (2002).
74. Li, J., Pawitwar, S. S. & Rosen, B. P. The organoarsenical biocycle and the primordial antibiotic methylarsenite. *Metallomics* **8**, 1047–1055 (2016).
75. Giovannoni, S. J. et al. A parasitic arsenic cycle that shuttles energy from phytoplankton to heterotrophic bacterioplankton. *mBio* **10**, e00246-19 (2019).
76. Konhauser, K. O. et al. Oceanic nickel depletion and a methanogen famine before the Great Oxidation Event. *Nature* **458**, 750–753 (2009).
77. Li, Y. P. et al. Antimicrobial activity of metals and metalloids. *Annu. Rev. Microbiol.* **75**, 175–197 (2021).
78. Mukherjee, I., Corkrey, R., Large, R. & Danyushevsky, L. Abiotic and biotic constraints on Earth's ancient colonisers in the Proterozoic. *Precambrian Res.* **393**, 107089 (2023).
79. Mustafa, A. et al. Nickel (Ni) phytotoxicity and detoxification mechanisms: a review. *Chemosphere* **328**, 138574 (2023).
80. Rostami, S. & Azhdarpoor, A. The application of plant growth regulators to improve phytoremediation of contaminated soils: a review. *Chemosphere* **220**, 818–827 (2019).
81. Wilson, M. C. et al. An environmental bacterial taxon with a large and distinct metabolic repertoire. *Nature* **506**, 58–62 (2014).
82. Keren, R. et al. Sponge-associated bacteria mineralize arsenic and barium on intracellular vesicles. *Nat. Commun.* **8**, 14393 (2017).
83. Orani, A. M., Barats, A., Zitte, W., Morrow, C. & Thomas, O. P. Comparative study on the bioaccumulation and biotransformation of arsenic by some northeastern Atlantic and northwestern Mediterranean sponges. *Chemosphere* **201**, 826–839 (2018).
84. Edmonds, J. S. et al. Isolation, crystal structure and synthesis of arsenobetaine, the arsenical constituent of the western rock lobster *Panulirus longipes cygnus* George. *Tetrahedron Lett.* **18**, 1543–1546 (1977).
85. Gaion, A., Sartori, D., Scuderi, A. & Fattorini, D. Bioaccumulation and biotransformation of arsenic compounds in *Hediste diversicolor* (Muller 1776) after exposure to spiked sediments. *Environ. Sci. Pollut. Res.* **21**, 5952–5959 (2014).
86. Yang, Y., Xie, X., Chen, M., Xie, Z. & Wang, J. Effects of sulfide input on arsenate bioreduction and its reduction product formation in sulfidic groundwater. *IJERPH* **19**, 16987 (2022).
87. Saleh, F., Daley, A. C., Lefebvre, B., Pittet, B. & Perrillat, J. P. Biogenic iron preserves structures during fossilization: a hypothesis: iron from decaying tissues may stabilize their morphology in the fossil record. *BioEssays* **42**, 1900243 (2020).
88. Janssen, K., Mähler, B., Rust, J., Bierbaum, G. & McCoy, V. E. The complex role of microbial metabolic activity in fossilization. *Biol. Rev.* **97**, 449–465 (2022).
89. Odin, G. P., Leloup, J., Nguyen Tu, T. T., Charbonnier, S. & Derenne, S. Taphonomic experiments on caridean shrimp elucidate the timing and influence of organic matter on diagenetic pyritization and sulfuration. *Chem. Geol.* **644**, 121858 (2024).
90. Carignan, J., Hild, P., Mevelle, G., Morel, J. & Yeghicheyan, D. Routine analyses of trace elements in geological samples using flow injection and low pressure on-line liquid chromatography coupled to ICP-MS: a study of geochemical reference materials BR, DR-N, UB-N, AN-G and GH. *Geostand. Newsl.* **25**, 187–198 (2001).
91. Bankole, O. M., El Albani, A., Meunier, A., Poujol, M. & Bekker, A. Elemental geochemistry and Nd isotope constraints on the provenance of the basal siliciclastic succession of the middle Paleoproterozoic Francevillian Group, Gabon. *Precambrian Res.* **348**, 105874 (2020).
92. McLennan, S. M. Relationships between the trace element composition of sedimentary rocks and upper continental crust. *Geochem. Geophys. Geosyst.* **2**, 2000GC000109 (2001).
93. Algeo, T. J. & Tribovillard, N. Environmental analysis of paleoceanographic systems based on molybdenum–uranium covariation. *Chem. Geol.* **268**, 211–225 (2009).
94. McLennan, S. M., Hemming, S., McDaniel, D. K. & Hanson, G. N. Geochemical approaches to sedimentation, provenance, and tectonics. in *Geological Society of America Special Papers* vol. 284 21–40 (Geological Society of America, 1993).
95. Panahi, A., Young, G. M. & Rainbird, R. H. Behavior of major and trace elements (including REE) during Paleoproterozoic pedogenesis and diagenetic alteration of an Archean granite near Ville Marie, Québec, Canada. *Geochim. Cosmochim. Acta* **64**, 2199–2220 (2000).
96. Somogyi, A. et al. Optical design and multi-length-scale scanning spectro-microscopy possibilities at the Nanoscopy beamline of Synchrotron Soleil. *J. Synchrotron Rad.* **22**, 1118–1129 (2015).
97. Wilson, S. A., Ridley, W. I. & Koenig, A. E. Development of sulfide calibration standards for the laser ablation inductively-coupled

- plasma mass spectrometry technique. *J. Anal. Spectrom.* **17**, 406–409 (2002).
98. Boström, K., Peterson, M. N. A., Joensuu, O. & Fisher, D. E. Aluminum-poor ferromanganese sediments on active oceanic ridges. *J. Geophys. Res.* **74**, 3261–3270 (1969).

Acknowledgements

We thank the French government program “Investissements d’Avenir” (EUR INTREE, reference ANR-18-EURE-0010), the Synchrotron SOLEIL, La Région Nouvelle Aquitaine (DEE21-28-2022-22881020), and the European Research Council (ERC) Seventh Framework (F7) program, grant No: 336092, for their financial support. F.S.’s work is supported by an SNF Ambizione Grant (PZ00P2_209102). We also thank the CENAREST Gabonais, the COMILOG and SOCOBA Companies, the French Embassy in Libreville, and the Institut Français du Gabon, for their support. We appreciate the technical and logistical help of C. Lebailly, A. Ngomanda, C. Laforest, E. Dondoglio, J. Ikouanga, A. Meunier, F. Parrotin, C. Boisard, R. Oslisly, S. Ventalon, and A. Trenteseaux. For the loan of fossiliferous nodules, property of the National Museum of Natural History of Paris (MNHN) and preserved at the Natural History Museum of Autun (MHNA), we thank S. Charbonnier, in charge of the collection at the MNHN, and A. Medina, curator of the MHNA. We also thank D. Sotty, inventor of the collection. This work is dedicated to the memory of Stefan Bengtson.

Author contributions

A.E.A. conceived and headed the project. A.E.K., A.S., E.C.F., F.S. and A.E.A. wrote the paper. A.E.K., A.E.A. and E.C.F. did the field work. A.E.K., A.S., C.F., M.H. and A.E.A. prepared the samples. A.E.K., A.S. and I.C. performed XRF and XANES analyses and models. C.R.B. and J.A. performed laser ablation. All authors discussed the results and reviewed the paper.

Competing interests

The authors declare no competing interests.

Additional information

Supplementary information The online version contains supplementary material available at <https://doi.org/10.1038/s41467-025-59760-9>.

Correspondence and requests for materials should be addressed to Farid Saleh or Abderrazak El Albani.

Peer review information *Nature Communications* thanks Nicolas Tribouillard and the other, anonymous, reviewer(s) for their contribution to the peer review of this work. A peer review file is available.

Reprints and permissions information is available at <http://www.nature.com/reprints>

Publisher’s note Springer Nature remains neutral with regard to jurisdictional claims in published maps and institutional affiliations.

Open Access This article is licensed under a Creative Commons Attribution-NonCommercial-NoDerivatives 4.0 International License, which permits any non-commercial use, sharing, distribution and reproduction in any medium or format, as long as you give appropriate credit to the original author(s) and the source, provide a link to the Creative Commons licence, and indicate if you modified the licensed material. You do not have permission under this licence to share adapted material derived from this article or parts of it. The images or other third party material in this article are included in the article’s Creative Commons licence, unless indicated otherwise in a credit line to the material. If material is not included in the article’s Creative Commons licence and your intended use is not permitted by statutory regulation or exceeds the permitted use, you will need to obtain permission directly from the copyright holder. To view a copy of this licence, visit <http://creativecommons.org/licenses/by-nc-nd/4.0/>.

© The Author(s) 2025